Chapter Five *Results and Discussion*

This chapter presents the results and the discussion from the modeling and simulation of the 1.55 μm VCSELs. The simulation work and results obtained are divided separately into DBR mirror and active region components. HS_Design Version 1.0 is used to study VCSELs DBR mirror and active region components. Based on the results, a 1.55 μm VCSELs device is then proposed and characterized. LaserMOD Version 2.0 is used for complete VCSELs device characteristic simulation.

5.1 DBR Mirror Component

As for the DBR mirror studies, three types of material system are examined that are InGaAsP/InP, GaAs/AlGaAs and SiC/MgO which each representing the epitaxially-grown, wafer-fused and dielectric-deposited mirror, respectively. All are quarter wave mirror with the thickness for each material layer is given by [46]

$$d = \frac{\lambda}{4n} \tag{5.1}$$

where d is the quarter wave layer thickness, λ is the design wavelength and n is the refractive index of the alloy at design wavelength. The high reflectivity or stopband of a DBR depends on the difference in refractive index of the two adjacent materials used, Δn. The spectral width of the stopband is given by [95]

$$\Delta\lambda_{stopband} = \frac{2\lambda_{Bragg}\Delta n}{\pi n_{eff}} \tag{5.2}$$

where maximum reflectivity occurred at Bragg wavelength, λ_{Bragg} and n_{eff} is the effective refractive index of the mirror calculated as [46]

$$n_{eff} = 2\left(\frac{1}{n_1} + \frac{1}{n_2}\right)^{-1} \tag{5.3}$$

5.1.1 *InGaAsP/InP DBR Mirror Simulation*

InGaAsP/InP material system is chosen to study for epitaxially-grown mirror because it is lattice-matched to the InGaAsP material which is mostly used in the active region of laser device at 1.55 μm wavelength. Table 5.1 listed the internal parameters used for the simulation of n-DBR InGaAsP/InP mirror. The thickness for each layer, *d* is calculated from equation (5.1) with other parameters are taken from the highest performance 1.55 μm VCSELs employing this type of mirror [49]. Figure 5.1 shows simulation result for various y composition levels in the InGaAsP quaternary material for the n-DBR InGaAsP/InP mirror. As the y composition increased, the reflectivity spectrum shifts towards longer wavelength. Maximum reflectivity, R_{max} and reflectivity at 1.55 μm, $R_{1.55}$ also becomes higher as shown in Figure 5.2. Figure 5.3 shows the wavelength of R_{max} and the stopband are increased linearly as the composition is increased. The period effect is also simulated for the DBR mirror. Figure 5.4 show that higher reflectivity is achieved as the period is added up. Maximum reflectivity, R_{max} and reflectivity at 1.55 μm, $R_{1.55}$ increased with period addition as exhibited in Figure 5.5 and Figure 5.6.

Table 5.1: Internal parameters of n-DBR InGaAsP/InP mirror.

Layer type	Material	Thickness, d (nm)	Doping Concentrations, N_d ($\times 10^{17}$ cm^{-3})	Refractive Index (n) at 1.55 μm	Repetition
superstrate	n-InP	180	50	3.17	
n-DBR	n-$In_{(1-x)}Ga_{(x)}As_{(y)}P_{(1-y)}$	112.3	50	3.45	50
	n-InP	122.2	50	3.17	
	n-$In_{(1-x)}Ga_{(x)}As_{(y)}P_{(1-y)}$	112.3	50	3.45	
substrate	n-InP	5000	50	3.17	

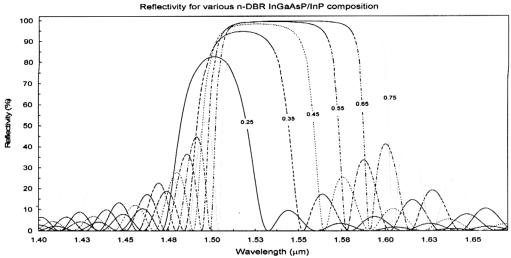

Figure 5.1: Reflectivity for various n-DBR InGaAsP/InP composition.

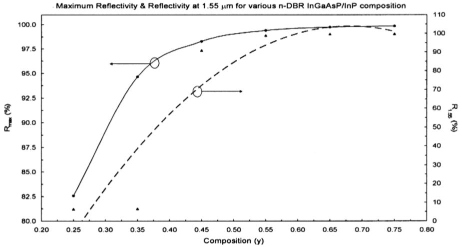

Figure 5.2: R_{max} and $R_{1.55}$ for various n-DBR InGaAsP/InP composition.

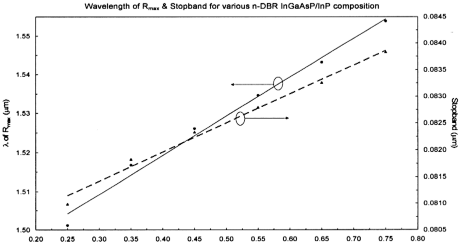

Figure 5.3: Wavelength of R_{max} and Stopband for various n-DBR InGaAsP/InP composition.

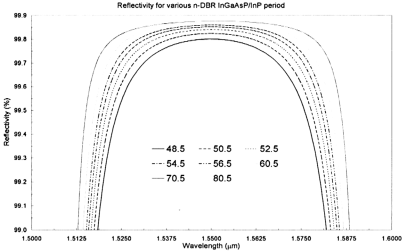

Figure 5.4: Reflectivity for various n-DBR InGaAsP/InP period.

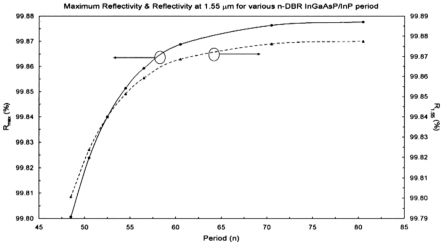

Figure 5.5: R_{max} and $R_{1.55}$ for various n-DBR InGaAsP/InP period.

The results and analysis of both the composition and period simulation of n-DBR InGaAsP/InP are also similar for p-DBR InGaAsP/InP simulation as shown in Figure 5.6-5.10. The p-DBR InGaAsP/InP mirror internal parameters taken from reference [49] is given in Table 5.2 except for the thickness, *d* which is from calculation.

Table 5.2: Internal parameters of p-DBR InGaAsP/InP mirror.

Layer type	Material	Thickness, d (nm)	Doping Concentrations, N_d (x10^{17}cm^{-3})	Refractive Index (n) at 1.55 μm	Repetition
superstrate	p-InP	180	50	3.17	
p-DBR	p-$In_{(1-x)}Ga_{(x)}As_{(y)}P_{(1-y)}$	112.3	10	3.45	50
	p-InP	122.2	10	3.17	
	p-$In_{(1-x)}Ga_{(x)}As_{(y)}P_{(1-y)}$	112.3	10	3.45	
substrate	p-InP	5000	50	3.17	

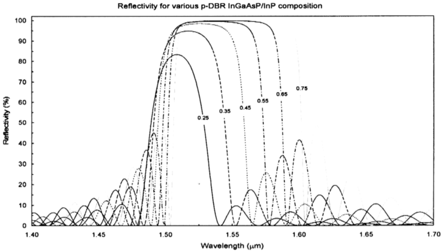

Figure 5.6: Reflectivity for various p-DBR InGaAsP/InP composition.

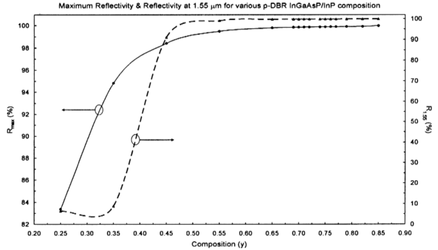

Figure 5.7: R_{max} and $R_{1.55}$ for various p-DBR InGaAsP/InP composition

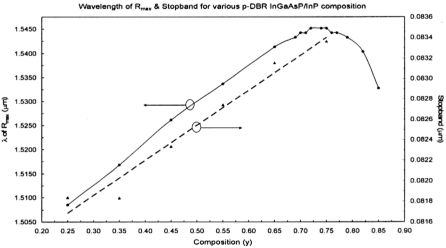

Figure 5.8: Wavelength of R_{max} and Stopband for various p-DBR InGaAsP/InP composition.

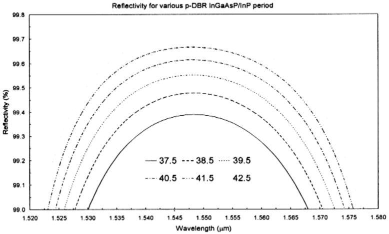

Figure 5.9: Reflectivity for various p-DBR InGaAsP/InP period.

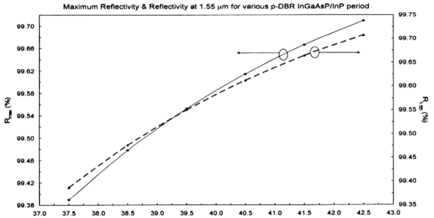

Figure 5.10: R_{max} and $R_{1.55}$ for various p-DBR InGaAsP/InP period.

5.1.2 *GaAs/AlGaAs DBR Mirror Simulation*

GaAs/AlGaAs material system is recently developed as wafer-fusion DBR mirror with InGaAsP active region for 1.55 μm VCSEL. For the simulation, the internal parameters listed in Table 5.3 are based on the optimized reported work [101] for the 1.55 μm VCSELs except for the thickness, *d* which is calculated from equation (5.1).

Table 5.3: Internal parameters of n-DBR GaAs/AlGaAs mirror.

Layer type	Material	Thickness, d (nm)	Doping Concentrations, N_d ($x10^{17}cm^{-3}$)	Refractive Index (n) at 1.55 μm	Repetition
superstrate	n-GaAs	50	10	3.37	
n-DBR	n-GaAs	115.0	10	3.37	30
	n-$Al_{(x)}Ga_{(1-x)}As$	127.5	10	3.04	
	n- GaAs	115.0	10	3.37	
substrate	n-GaAs	5000	50	3.37	

Figure 5.11 shows the reflectivity spectrum for various x compositions in the AlGaAs ternary material for the n-DBR GaAs/AlGaAs mirror. The reflectivity spectrum shifts towards shorter wavelength as the x composition increased. Figure 5.12 demonstrates the increment of maximum reflectivity, R_{max} and reflectivity at 1.55 μm, $R_{1.55}$ with the addition of the composition level. However, wavelength of R_{max} and the stopband are declining linearly as the composition is increased as shown in Figure 5.13.

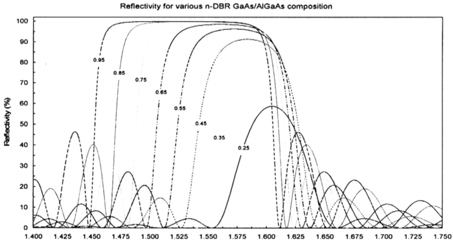

Figure 5.11: Reflectivity for various n-DBR GaAs/AlGaAs composition.

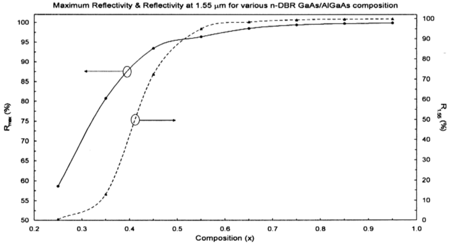

Figure 5.12: R_{max} and $R_{1.55}$ for various n-DBR GaAs/AlGaAs composition.

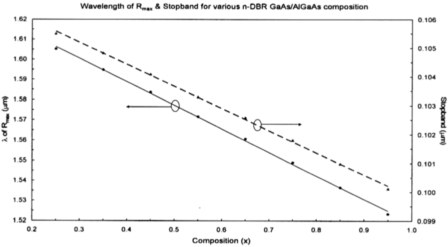

Figure 5.13: Wavelength of R_{max} and Stopband for various n-DBR GaAs/AlGaAs composition.

As for the period simulation, Figure 5.14 exhibits that higher reflectivity is achieved as the period is added up. Maximum reflectivity, R_{max} which occurred exactly at 1.55 µm also increased with period addition as shown in Figure 5.15. Thus, reflectivity at 1.55 µm, $R_{1.55}$ has the same value with R_{max}. The wavelength of R_{max} for various periods simulated is constant at 1.55 µm with the same value of stopband.

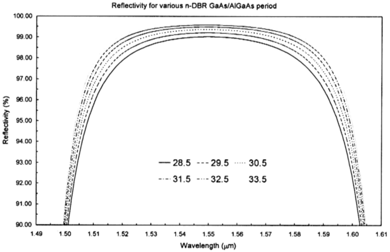

Figure 5.14: Reflectivity for various n-DBR GaAs/AlGaAs period.

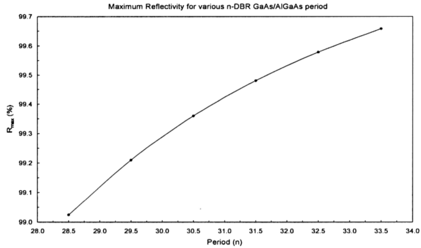

Figure 5.15: R_{max} for various n-DBR GaAs/AlGaAs period.

The composition and period simulation for p-DBR GaAs/AlGaAs mirror also demonstrated similar results as that for the n-DBR GaAs/AlGaAs mirror. Table 5.4 listed the internal parameters based on [101] with the thickness, *d* is calculated using equation (5.1). The simulation results are shown from Figure 5.16 to 5.20.

Table 5.4: Internal parameters of p-DBR GaAs/AlGaAs mirror.

Layer type	Material	Thickness, d (nm)	Doping Concentrations, N_d ($\times10^{17}$cm^{-3})	Refractive Index (n) at 1.55 μm	Repetition
superstrate	p-GaAs	184	4	3.37	
p-DBR	p-GaAs	115.0	4	3.37	30
	p-$Al_{(x)}Ga_{(1-x)}As$	127.5	4	3.04	
	p-GaAs	115.0	4	3.37	
substrate	p-GaAs	20	4	3.37	

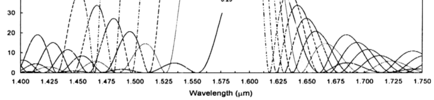

Figure 5.16: Reflectivity for various p-DBR GaAs/AlGaAs composition.

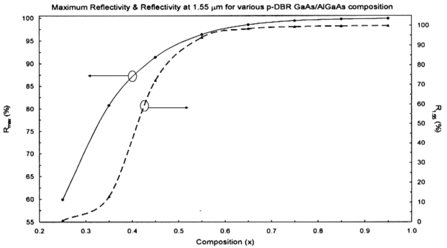

Figure 5.17: R_{max} and $R_{1.55}$ for various p-DBR GaAs/AlGaAs composition.

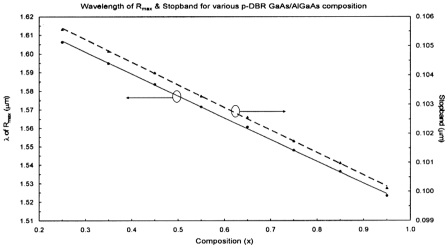

Figure 5.18: Wavelength of R_{max} and Stopband for various p-DBR GaAs/AlGaAs composition.

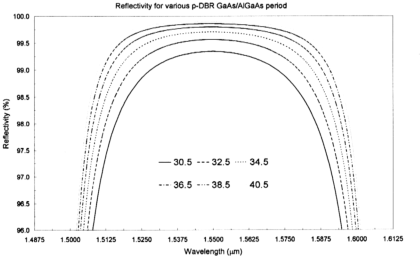

Figure 5.19: Reflectivity for various p-DBR GaAs/AlGaAs period.

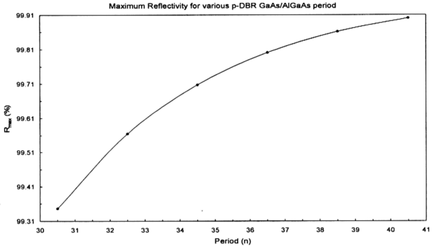

Figure 5.20: R_{max} for various p-DBR GaAs/AlGaAs period.

5.1.3 *SiC/MgO DBR Mirror Simulation*

SiC/MgO material system demonstrates high performance in term of thermal conductivity and low optical absorption among the amorphous semiconductors applied for dielectric-deposited VCSELs DBR mirror [57]. Table 5.5 listed the internal parameters for the simulation with the thickness; d is calculated from equation (5.1). Since no doping is needed for this type of material, the mirror can be employed either as p-type or n-type VCSELs DBR mirror.

Table 5.5: Internal parameters of SiC/MgO DBR mirror.

Layer type	Material	Thickness, d (nm)	Refractive Index (n) at 1.55 μm	Repetition
DBR	Si-C	150.8	2.57	10
	MgO	226.6	1.71	
	Si-C	150.8	2.57	

Figure 5.21(a) exhibits the reflectivity spectrum for various period of SiC/MgO DBR mirror with the magnification at the stopband shown in Figure 5.21(b), where higher reflectivity is obtained as the number of period is added up. Maximum reflectivity, R_{max} which occurred at 1.55 μm also increased with the period addition as shown in Figure 5.22. Thus, reflectivity at 1.55 μm, $R_{1.55}$ has the same value with R_{max}. The wavelength of R_{max} is fixed at 1.55 μm with a constant stopband.

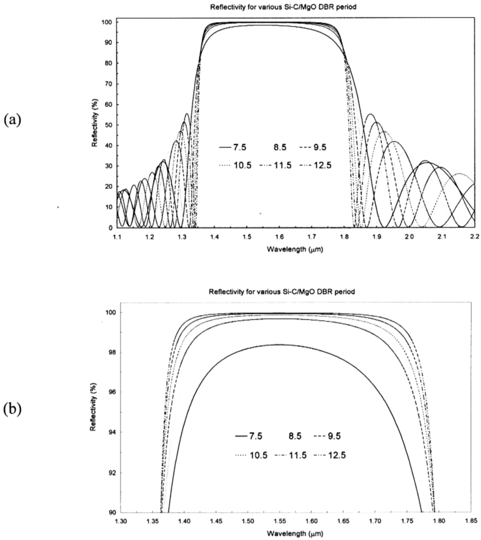

Figure 5.21: (a) Reflectivity for various SiC/MgO periods with (b) Stopband magnified.

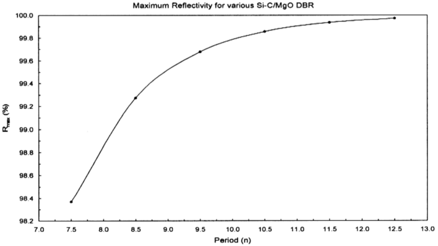

Figure 5.22: R_{max} for various SiC/MgO period.

5.1.4 *DBR mirror Discussion & 1.55 μm VCSELs DBR Mirror Proposed*

A high reflectivity mirror can be achieved by using a structure such as DBR in which the refractive index of every subsequent layer alternates. By spacing multiple high-to-low index interfaces a distance $\lambda/4$ apart, the reflected waves of each interface interfere constructively at the design frequency and produce mirrors with high reflectivity (>99%) with a phase exactly zero or π. Figure 5.23 shows a schematic illustration of the principle of DBR mirror. The reflection coefficient r_{12} for wave in layer 1 being reflected at the 1-2 boundary is $r_{12} = (n_1 - n_2) / (n_1 + n_2)$ and is a negative number indicating a π phase change. The reflection coefficient for wave in layer 2 being reflected at the 2-1 boundary is $r_{21} = (n_2 - n_1) / (n_1 + n_2)$ which is $-r_{12}$ (positive) indicating no phase change. Thus, the reflection coefficient alternates in sign through the DBR mirror. Consider two arbitrary waves A and B which are reflected at two consecutive interfaces. The two waves are therefore already out of phase by π due to reflections at the different boundaries. In further, wave B travels an additional distance which is twice ($\lambda_2/4$) before reaching wave A and experiences a phase change equivalent to $2(\lambda_2/4)$ or $\lambda_2/2$, that is π. The phase difference between A and B is then $\pi+\pi$ *or* 2π. Thus, waves A and B are in phase interfering constructively. Waves B and C also interfere constructively and so on, thus all the reflected waves from the consecutive boundaries interfere constructively. Multiple reflections at the DBR interfaces and constructive interference of the reflected waves increase the reflectivity with increasing number of pairs.

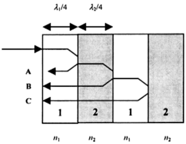

Figure 5.23: Schematic illustration of the principle of DBR mirror with alternate high and low refractive index layers and its reflectance.

The reflectivity spectrum of all the DBR mirror material systems simulated shows that the spectrum exhibit complicated phase and amplitude spectrum due to its distributed multi-reflection nature. The important portion of the mirror spectrum is at or in the surrounding of the anti-resonance frequency or called the center of the stopband region. The anti-resonance consists of the round trip phase within each layer in the mirror at frequency equals an odd multiple of π. The center frequency is also referred to as the Bragg frequency where the maximum reflectivity occurs. The spectrum is also periodic, where the high reflectivity stopband repeats every odd multiple of the Bragg frequency. Table 5.6 listed the optimum internal parameters and results obtained from the simulation of each DBR mirror types.

Table 5.6: Optimum internal parameters and results for each DBR simulation.

Type / Parameter	n-DBR			p-DBR		
	InGaAsp/InP	GaAs/AlGaAs	SiC/MgO	InGaAsp/InP	GaAs/AlGaAs	SiC/MgO
Refractive Index	3.45/3.17	3.37/3.04	2.57/1.71	3.45/3.17	3.37/3.04	2.57/1.71
Period (n)	-	41.5	11.5	39.5	33.5	9.5
Thickness, d (μm)	-	10.1	4.3	9.3	8.1	3.5
Doping Concentrations, N_d (x10^{17}cm^{-3})	-	10 / 10	-	10 / 10	4 / 4	-
Composition	-	x=0.72	-	y=0.750 x=0.348	x = 0.74	-
R_{max} (%)	-	99.91	99.94	99.65	99.66	99.68
Wavelength of R_{max} (μm)	-	1.55	1.55	1.55	1.55	1.55
Stopband (nm)	-	101.9	413.2	83.6	101.9	413.2
Absorption Coefficient at 1.55 μm (1/cm)	-	15.1	22.4	41.6	23.4	22.4

All of the mirror systems exhibit highest reflectivity at 1.55 μm which corresponds to the emission wavelength of the VCSELs device. There is no optimized result for n-DBR InGaAsP/InP mirror because the reflectivity achieved is only 99.8% even by applying 80.5 periods. The minimum reflectivity needed for n-DBR mirror is 99.9%. Furthermore, the 80.5 periods produced a DBR with 18.9 μm thickness which is not applicable for VCSELs fabrication as will be described later on. For a comparison, Figure 5.24 shows the reflectivity spectrum of each DBR mirror type, using the p-DBR as a general comparison due to the results similarity between p- and n-DBR mirrors for each material system. From the results, the maximum reflectivity, $R_{\max}$ for each of the p-DBR material is plot against the number of period as exhibited in Figure 5.25

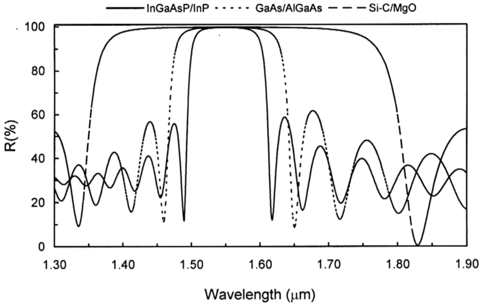

Figure 5.24: Reflectivity spectrum for different p-DBR mirror material system.

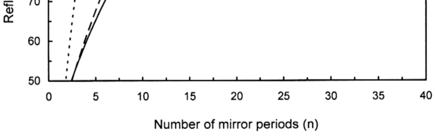

Figure 5.25: $R_{\max}$ versus number of periods for different p-DBR mirror material system.

The relatively small index contrast between InGaAsP and InP (Δn~0.28) required a growth of large number of mirror periods (>50 periods [49]) before reaching high reflectivity. This challenges the growth technology, because the growth time may approach long hours and also the growth platform must be extremely stable to obtain a uniform DBR layer thickness. Besides, the quarter wave layer thickness is larger at higher wavelength, thus each mirror layer will be thicker. Based on the 39.5 period obtained for p-DBR InGaAsP/InP mirror, the entire structure becomes 9.26 μm. It results a thick device for one part of the mirror itself, thus increasing the electrical resistance. Thick InGaAsP/InP DBR will also block the thermal flux to the heat sink which can lead to a strong increase of the active region temperature. The small index contrast also produces large penetration depth into the mirror increasing diffractive and absorption losses, which reducing the mirror reflectivity [53].

GaAs/AlGaAs material system has high refractive index ratio (Δn~0.33), thus fewer periods are required as shown in Figure 5.25. This material system exhibits high electrical conductivity and have the highest thermal conductance for epitaxial-grown mirror [48]. This material system would be a good choice in 1.55 μm VCSELs. Nevertheless, due to the lattice mismatch, GaAs/AlGaAs mirror cannot be grown on InGaAsP active region for long wavelength application. Other critical problem is that the constraints on p-type doping level at longer wavelengths, where free-carrier absorption and intervalence band absorption in GaAs both increase dramatically below the bandgap for extrinsic p-type GaAs [53]. However, this can be overcome by using high active region gain.

The SiC/MgO material combination, in contrast, requires even fewer numbers of periods because the refractive index ratio is much larger between the two materials (Δn~0.79). This high contrast means only small number of periods is needed to achieve high reflectivity, allowing for smaller devices to be fabricated. This does produce DBR with very high reflectivity but, due to its insulating dielectric nature, a complicated current scheme is required. Furthermore, in amorphous semiconductors the absorption tail extends deep into the forbidden gap [102], hence the reflectivity of these mirrors is limited by high material absorption.

In addition to a decrease in peak reflectivity, the width of the stopband shrinks with a decreasing refractive index contrast as indicated in equation (5.4) and (5.5), respectively [98]. $R_{\max}$ is the maximum reflectivity at the stopband center, $\Delta\omega$ is the stopband frequency bandwidth, ω_0 is the center frequency of the stopband, n_H and n_L are the high- and low-refractive index layer, and n_0 and n_S are the refractive index of the incident medium and the substrate, respectively.

$$R_{max} = \left(\frac{1 - \left(\frac{n_S}{n_0}\right)\left(\frac{n_H}{n_L}\right)^{2N}}{1 + \left(\frac{n_S}{n_0}\right)\left(\frac{n_H}{n_L}\right)^{2N}} \right)^2 \tag{5.4}$$

$$\Delta\omega = \frac{4\omega_0}{\pi} \arcsin\left(\frac{n_H - n_L}{n_H + n_L}\right) \tag{5.5}$$

This in turn causes decreased tolerance on the growth of the VCSELs structure [27]. Errors in the thickness of the cavity result in a shifting of the lasing peak within the DBR stopband. Thus, the narrower the stopband which occurs for a lower refractive index contrast allows for less tolerance in fabrication process. The stopband also act as a control mechanism to design the laser output at a specific wavelength.

Figure 5.26 shows the absorption coefficient for each material system of the DBR mirror in the range of 1.4 µm to 1.75 µm. The absorption coefficient at 1.55 µm is listed for each DBR mirror system in Table 5.6. The absorption loss at 1.55 µm is high for InGaAsP/InP system because of Auger nonradiative recombination and higher intervalence band absorption [53]. Absorption loss in GaAs/AlGaAs system is mostly contributed by free-carrier absorption and intervalence band absorption [53]. As for SiC/MgO system, it is due to high material absorption [102].

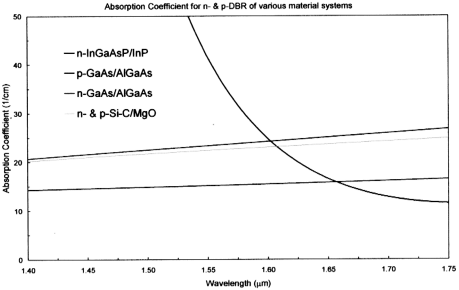

Figure 5.26: Absorption coefficient simulation for various n- & p-DBR material systems in the range of 1.4 μm to 1.75 μm.

Another consideration of the DBR mirror for longer wavelength VCSELs is its thermal properties. Since the VCSELs have such small volume and require higher current densities than EELs, it can generate quite a bit of heat in the active region. This can shift the cavity mode as well as the gain peak of the active region toward longer wavelengths at different rates. This difference in rates causes the gain peak to slide off from the cavity mode, thus producing no output power and finally a shut down of the VCSELs emission. Due to this factor, it is important for VCSELs to dissipate heat efficiently through the DBR mirror. However, not all DBR mirror materials dissipate heat equally well. In general, thermal conductivity, *k* of binary alloys is superior to ternary alloys, which in turn better than the quaternary alloys due to the disorder scattering of phonons [48]. Despite such poor thermal conductivity for ternary and quaternary alloys, both are still better than dielectric materials with exception of SiC/MgO which has good thermal conductivity as reported [57].

Based on the simulation and results obtained, GaAs/AlGaAs DBR mirror has many advantages compared with InGaAsP/InP and SiC/MgO material systems. It meets the DBR requirements which are highly reflective and have high electrical and thermal conductivity. It is suggested to employ GaAs/AlGaAs material system as n- and p-DBR mirror for the proposed 1.55 μm VCSELs diode. The highest long wavelength VCSELs to date [63] also employs the same material system for the DBR mirror.

5.2 Active Region Component

The material studies such as strain effect, composition level, well thickness and the number of QW of active region are important for the VCSELs to produce high gain active region. This will compensate for losses in the DBR cavity due to low reflectivity, diffraction and absorption. InGaAsP material system is employed in the simulation because it is extensively used for 1.3 to 1.55 μm applications. Table 5.7 listed the internal parameters taken from [103].

Table 5.7: Internal parameters for InGaAsP active region simulation.

Layer type	Thickness, d (nm)	Composition		Repetition
		x	y	
QW	0.3	0.238	0.82	6
Barrier	8.0	0.382	0.82	
QW	0.3	0.238	0.82	

5.2.1 *Strain Effect Simulation*

Figure 5.27 displays optical gain for the InGaAsP active region with different compressive strain percentage applied to the QW layer. The gain is increased as the strain percentage become higher. Figure 5.28 shows that the gain at 1.55 μm wavelength, $G_{1.55}$ is also increasing linearly.

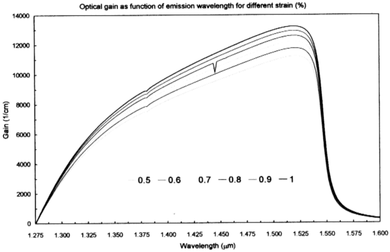

Figure 5.27: Optical gain as function of emission wavelength for different strain (%).

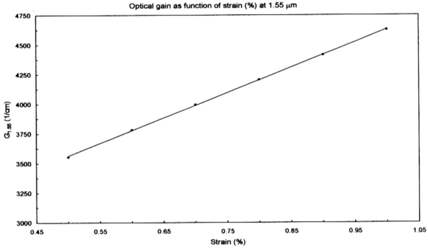

Figure 5.28: Optical gain as function of strain (%) at 1.55 μm.

5.2.2 *Composition Effect Simulation*

The optical gain shift towards longer wavelength with increasing composition level as shown in Figure 5.29. From Figure 5.30, gain at 1.55 μm, $G_{1.55}$ is also increased within the composition increment. However after 0.85 y composition, it decreases as exhibited in Figure 5.30. Maximum gain, G_{max} at this composition level (y=0.85) is obtained at the targeted 1.55 μm wavelength as can be shown in Figure 5.31. The position of maximum gain G_{max} increases linearly with increasing Arsenic composition as shown in the Figure 5.31.

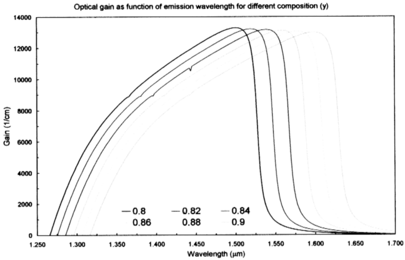

Figure 5.29: Optical gain as function of emission wavelength for different composition (y).

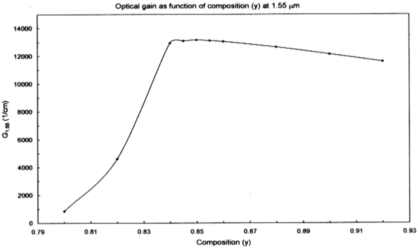

Figure 5.30: Optical gain as function of composition (y) at 1.55 µm.

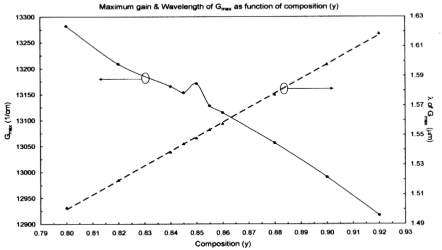

Figure 5.31: G_{max} and wavelength of G_{max} as function of composition (y).

5.2.3 *Quantum Well Thickness Effect Simulation*

Figure 5.32 exhibited the optical gain as function of emission wavelength for different QW thickness. As QW thickness is increased, the optical gain will become lower as exhibited in Figure 5.32. This also linearly decreases the gain at 1.55 μm, $G_{1.55}$ as shown in Figure 5.33.

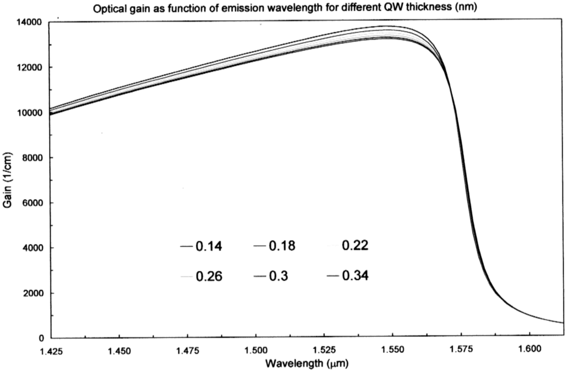

Figure 5.32: Optical gain as function of emission wavelength for different QW thickness (nm).

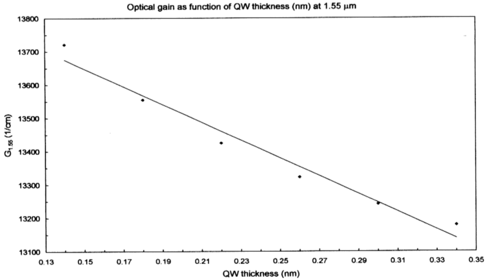

Figure 5.33: Optical gain as function of QW thickness (nm) at 1.55 μm.

5.2.4 *Number of Quantum Well Effect Simulation*

An increase in the number of QW will produced a higher optical gain as simulated in Figure 5.34. This will also give the same effect in gain at 1.55 μm wavelength, $G_{1.55}$ as shown in Figure 5.35. Figure 5.36 demonstrated that the maximum gain, G_{max} is increasing linearly, as well as its wavelength, where it is shifting towards longer wavelength when the number of QW is added.

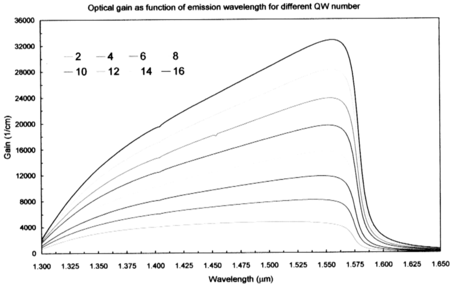

Figure 5.34: Optical gain as function of emission wavelength for different QW number.

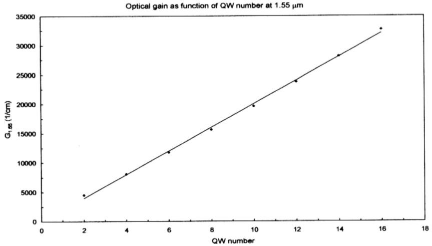

Figure 5.35: Optical gain as function of QW number at 1.55 μm.

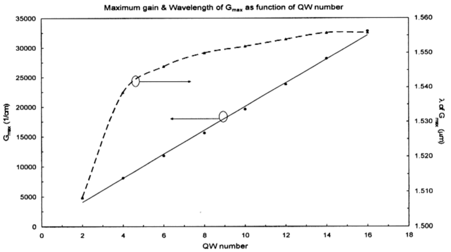

Figure 5.36: G_{max} and wavelength of G_{max} as function of QW number.

5.2.5 *Active Region Discussion & 1.55 µm VCSELs Active Region Proposed*

The optical gain in the active region can become higher by employing compressively strain QW. Results from the strain effect simulation show that optical gain is increasing with the percentage of strain applied. Strain can be applied as a compressive strain (atoms in the layer are forced together) or as a tensile strain (atoms in the layer are pulled apart) to match the crystalline structure of two lattice mismatch material. Figure 5.37 shows the effects of strain and unstrained layer.

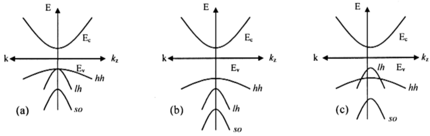

Figure 5.37: Schematic band structure for (a) unstrained layer (b) compressive strained layer and (c) tensile strained layer.

The active region is unstrained in Figure 5.37(a) showing the normal band structure. Figure 5.37(b) and 5.37(c) shows the effect of compressive strain and tensile strain, respectively. For QW applying compressive strain, the valence bands are split and the bandgap becomes wider as the valence bands are pulled further apart. This extends the energy separation between the heavy-hole valence band, *hh* with light-hole valence band, *lh* and split-off valence band, *so*. A larger density of holes can be accommodated in the top valence band itself before the next band is populated. As a result, the top *hh*-band is increasingly populated by holes as the number of holes transit from *so*- and *lh*-band to conduction band decreases. Thus, the optical gain is higher for increasing percentage of strain as the top *hh*-band is controlled by the compressive strain applied to the QW. As for the proposed 1.55 μm VCSELs, it is proposed to apply 1% of compressive strain and -0.9% of tensile strained barriers for the QWs. These parameters are based on the highest performance 1.55 μm VCSELs reported [63].

The composition effect simulation results show that both Ga and As compositions can be engineered to tailor the emission wavelength required. Material composition and strain in QW are not the independent parameters. For quaternary compounds of $In_{1-x}Ga_xAs_yP_{1-y}$, the mole fractions of the Ga and As and the QW strain parameter are related using equation (5.4) from [86], where δ is the strain expressed in %. Compressive strain is valued positively while tensile strain is valued negatively. Maximum optical gain is achieved at the designed 1.55 μm wavelength by employing composition level of x=0.25 and y=0.85 for the InGaAsP material.

$$x = \frac{0.1896y - 5.8688\times10^{-2}\delta[\%]}{0.4176 - 0.0125y} \tag{5.6}$$

As for the QW thickness simulation results, it demonstrated that the optical gain obtained decreased as the QW thickness is increased. When two materials with lattice mismatch are applying strain, one material will be distorted and enormous elastic energy builds up. Only a thin material can tolerate such stress. If the material becoming too thick, relaxation can occurs with the material intend to return into its original lattice constant. A defect will appear which is called misfit dislocation where many bonds are broken to relieve the strain in the over layer. This dislocation can create chain reaction from the QW which end on the surface of the outmost layer. This can degrade the optical and electronic properties of the device, thus reducing the laser diode performance. In an epitaxial layer, there exists a maximum critical layer thickness depending on the material which is proportional to the elastic energy created in a strained layer [104]. Above this thickness, the misfit dislocation will occur.

Besides applying strain, higher optical gain in the active region can also be produced by employing more number of QW as simulated in the number of QW effect study. However, complexity arises if using very high number of QW. The QW must be designed in an appropriate place in the cavity to maximize the overlap with the standing electric field of the device. Higher numbers of QW are also known to reduce Auger recombination but will increase QW absorption losses as in EELs [64]. Currently, active region with seven to twelve compressively strained QWs are employed in most long wavelength VCSELs [49, 58, 62, 105-106]. From the simulation results, maximum optical gain is achieved at the targeted 1.55 μm wavelength by applying only eight QW.

Table 5.8 listed the proposed internal parameters for the InGaAsP active region based from all the simulation results obtained. This active region employed eight QW with compressive strain of 1% and seven barriers with tensile strain of -0.9%, with respective composition shown below.

Table 5.8: Internal parameters for proposed InGaAsP active region simulation.

Layer type	Thickness, d (nm)	Composition		Repetition
		x	y	
QW	0.15	0.252	0.85	7
Barrier	8.0	0.396	0.85	
QW	0.15	0.252	0.85	

The optical gain is simulated as a function of wavelength, carrier density and temperature, g (λ, N, T). In EELs, the emission wavelength is achieved at the maximum gain peak wavelength given by $\lambda_e=\lambda_{max}$ since the longitudinal optical mode spacing is very small where the mode with the highest gain produced the lasing. In VCSELs, the longitudinal mode spacing is much wider due to the short cavity. The emission wavelength λ_c is given by the optical cavity and the gain-offset λ_{max}-λ_e depending on the temperature. As the temperature changes, the gain peak wavelength, λ_{max} shifts due to the changing bandgap. Figure 5.38 shows the optical gain for the proposed active region at various carrier density, *N* and at temperature, *T*=300K. The optical gain at 1.55 μm wavelength, $G_{1.55}$ increases as the carrier density increasing as displayed in Figure 5.39. At lower carrier density, increasing band filling causes a blue-shift (towards shorter wavelength) of the gain peak wavelength and at higher current density, gain peak wavelength red-shift (towards longer wavelength) occurs where carrier exchange and correlation effects lead to bandgap shrinkage [103].

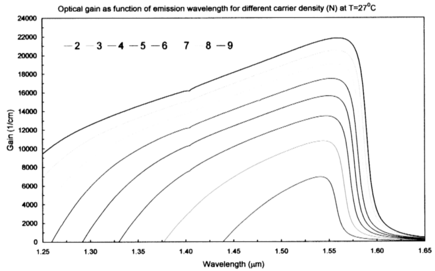

Figure 5.38: Optical gain as function of emission wavelength for different carrier density (x10^{18}cm^{-3}) at T=300K.

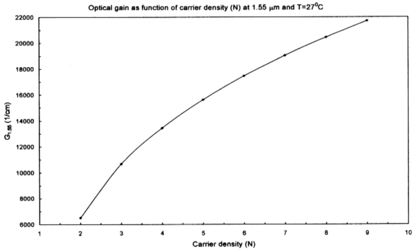

Figure 5.39: Optical gain as function of carrier density at 1.55 μm and T=300K.

Figure 5.40 displays the optical gain for the proposed active region at different temperature. The simulation is run at a fixed carrier density, N=5x10^{18}cm^{-3}. At lower temperature operation, the gain peak increases but its wavelength, λ_{gain} moves toward shorter wavelength. This blue-shift gain peak wavelength is due to the temperature dependence of the electron energy band gap. The increase of the gain peak is caused by a steeper Fermi distribution function of electrons [107]. MQW loss mechanisms like Auger recombination and intervalence band absorption are less important at low temperatures. The red-shift of the gain peak wavelength as the temperature rise can be attributed to intervalence band absorption and carrier leakage within the MQW [103]. The declined of the optical gain can be shown as in Figure 5.41 where the gain at 1.55 μm wavelength, $G_{1.55}$ decreased linearly with higher temperature operation. Also, at longer wavelength, Auger recombination is known to enhance non-radiative losses for InGaAsP active region [103]. With lower photon energy, electron transitions from the split-off valence band into empty states of the heavy-hole band occur at high hole densities, causing strong intervalence band absorption. Additional temperature effects might originate from thermionic emission at the fused interface and from changes of the carrier mobility [107].

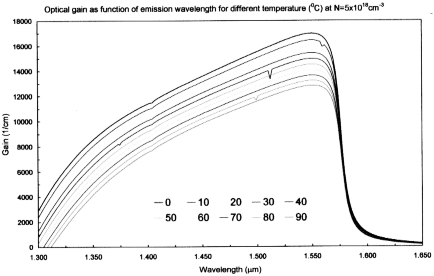

Figure 5.40: Optical gain as function of emission wavelength for different temperature (^{0}C) at N=5 x10^{18}cm^{-3}.

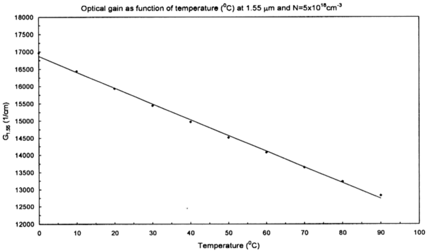

Figure 5.41: Optical gain as function of temperature at 1.55 μm and N=5 $x10^{18}cm^{-3}$.

From the entire optical gain spectrum simulation results exhibited above, there is a tail in the longer wavelength where the photon energy is smaller than the bandgap energy, in spite of the facts that no states are allowed within the bandgap energy. This is due to energy broadening caused by intraband relaxation [29] as calculated by the Lorentzian model used for the calculation. This Lorentzian broadening forms the tail in the optical gain spectrum where the effect on the gain spectrum has been discussed in detail [108-109].

In EELs diodes, the emission wavelength follows the gain peak. This is different in VCSELs, where the short vertical length of the cavity results in a single longitudinal optical mode at an emission wavelength, λ_{cav} which is given by the optical distance of the DBR. Due to the short optical resonator, the emission wavelength of a mode in VCSELs is determined by the cavity resonance and not by the gain peak as in conventional EELs diodes [107]. The gain peak decreased and shift towards longer wavelength for increasing temperature. The thermal wavelength shift is mainly dominated by changes of the mean refractive index in the resonator and another 10% by the thermal expansion of the semiconductor layers [27].

5.3 Proposed Device Design for 1.55 μm VCSELs Diode

Based on the DBR mirror and active region simulation results in sections 5.1 and 5.2 respectively, a full device design for 1.55 μm VCSELs diode is proposed for device characterization. From the DBR mirror results, 41.5 periods of GaAs/$Al_{0.72}Ga_{0.28}As$ with $1x10^{18}cm^{-3}$ doping forms the bottom n-DBR mirror. A total of 33.5 periods of GaAs/$Al_{0.74}Ga_{0.26}As$ with $4x10^{17}cm^{-3}$ doping is employed for the top p-DBR mirror. Both of these DBR mirrors are wafer-fused to the proposed InGaAsP active region consists of eight QW with 1.0% compressive strain and seven barriers with -0.9% tensile strain. This multi QW active region is embedded in InP spacer layers that have been extended by thin GaAs layers on each of the fused mirror to increase the emission wavelength. The parameters for both n- and p-spacer, n-GaAs substrate and Au/Ti contact is taken from the highest performance VCSELs [63] for 1.55 μm wavelength. The device diameter is 12 μm and the total thickness is 24.24522 μm. It has a 2 mm hole for light output at the top p-DBR mirror as demonstrated in the same reported VCSELs above [63]. The proposed 1.55 μm VCSELs diode structure is shown schematically in Figure 5.42(a) with the middle part is magnified as displayed in Figure 4.42(b). The entire device internal parameters are listed in Table 5.9.

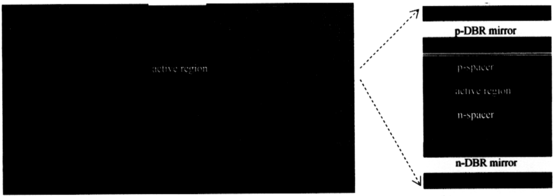

(a) (b)

Figure 5.42: (a) Schematic structure of the proposed 1.55 μm VCSELs diode with (b) middle structure is magnified.

Table 5.9: Schematic structure with the internal parameters for 1.55 μm VCSELs diode.

Layer type	Material	Thickness, d (nm)	Doping Concentrations, N_d (x10^{17}cm^{-3})	Repetition
p-contact	Au/Ti	200	undoped	
p-DBR	p-GaAs	115.0	4	33
	p-$Al_{0.74}Ga_{0.26}As$	127.5	4	
	p-GaAs	115.0	4	
p-spacer	p-GaAs	20	4	
	p-GaAs	10	400	
	p-InP	178	10	
	p-InP	100	0.1	
active region quantum well	$In_{0.748}Ga_{0.252}As_{0.85}P_{0.15}$	0.15	undoped	7
barrier	$In_{0.604}Ga_{0.396}As_{0.85}P_{0.15}$	8.0	undoped	
quantum well	$In_{0.748}Ga_{0.252}As_{0.85}P_{0.15}$	0.15	undoped	
n-spacer	n-InP	258	50	
	n-GaAs	50	10	
n-DBR	n-GaAs	115.0	10	41
	n-$Al_{0.72}Ga_{0.28}As$	127.5	10	
	n-GaAs	115.0	10	
substrate	n-GaAs	5000	5	
n-contact	Au/Ti	200	undoped	

5.4 1.55 μm VCSELs Diode Device Characterization

The device characterization simulation for the proposed 1.55 μm VCSELs diode above is done by using the LaserMOD version 2.0 software. The simulation characterized the device profile, mode analysis, photoluminescence (PL) spectra, emission spectrum and light-current-voltage (L-I-V) characteristic. Although full device dimension is calculated for the simulation, most of the results are only shown for x=0-6 μm or half-cut of the device diameter since the device structure is identical horizontally. As for the vertical direction, the simulation results of full device length for y=0-24.24522 μm is exhibited due to different material parameters applied.

5.4.1 *1.55 μm VCSELs Diode Device Profile*

In order to start the simulation of the device characteristic, the mesh points is firstly defined on the 1.55 μm VCSELs diode. This step is important to make the structure properly resolved. Figure 5.43 exhibited the mesh points generated where the active region and spacers structures have highly defined mesh to produce precise simulation results. Once the mesh is established, device profile such as refractive index profile, doping profile and energy band profile can be simulated. This is important to verify that the geometry and material parameters have been specified correctly for the proposed 1.55 μm VCSELs diode.

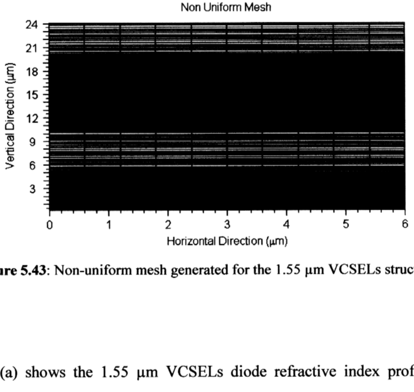

Figure 5.43: Non-uniform mesh generated for the 1.55 μm VCSELs structure.

Figure 5.44(a) shows the 1.55 μm VCSELs diode refractive index profile with the magnification in Figure 5.44(b). The difference in bandgap between the materials used in the proposed VCSELs produces a refractive index pattern as simulated in the profile. This refractive index profile provides light confinement or can be refer as optical waveguide in the device. Highest refractive index profile of 3.37 is achieved at y ≈15.60 μm which corresponds to the active region of the device.

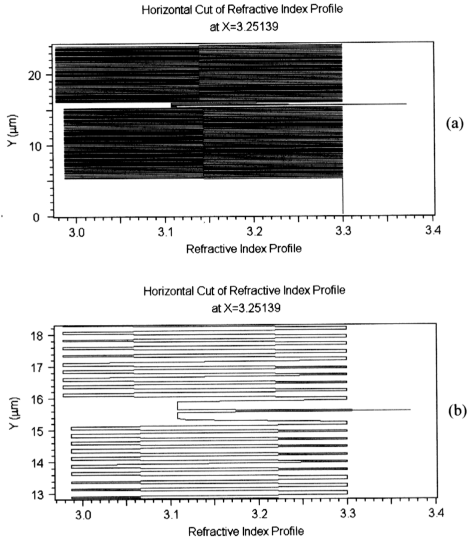

Figure 5.44: (a) Refractive index profile for the device structure and (b) with magnification.

Figure 5.45 shows the horizontal cut of net doping profile simulated for the 1.55 µm VCSELs diode. The donor doping and acceptor doping denotes the level of n- and p-type doping applied to the DBR mirror and the spacer layer. The zero value of the doping profile refers to the undoped active region. Figure 5.46(a) exhibits the 3D plot for the electron density inside the device which corresponds to the n-doping applied to the n-DBR mirror and n-spacer. The 3D plot of hole density illustrated in Figure 5.46(b) is referring to the p-DBR mirror and p-spacer which is p-doped.

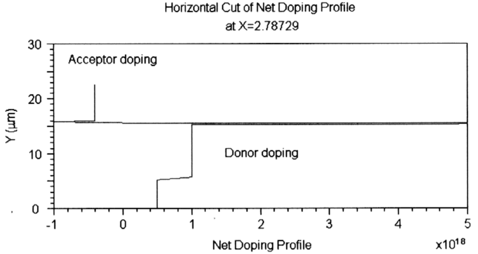

Figure 5.45: Net doping profile for the 1.55 µm VCSELs structure in horizontal cut.

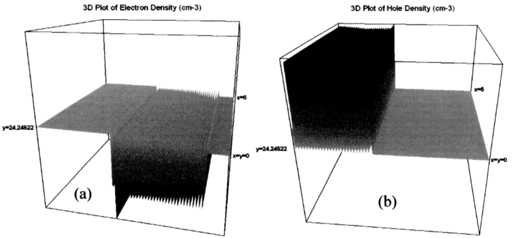

Figure 5.46: (a) Electron distribution and (b) Hole distribution inside the 1.55 µm VCSELs.

The simulation of 1.55 µm VCSELs energy band profile is run with two conditions that are at equilibrium (no applied bias) designate as Bias 0 and with a forward bias of 4 voltages designate as Bias 3. As described in Chapter Two, population inversion achieved by heavily doped both n- and p-region is needed to create stimulated emission in order to start the lasing operation. This heavy doping notably increases the potential barrier between the n- and p regions at equilibrium as shown in 3D plot of energy band in Figure 5.47(a). When a forward bias is applied, the potential barrier becomes lower as displayed in Figure 5.47(b), allowing electron-holes recombination with the emitted photons stimulate further emissions.

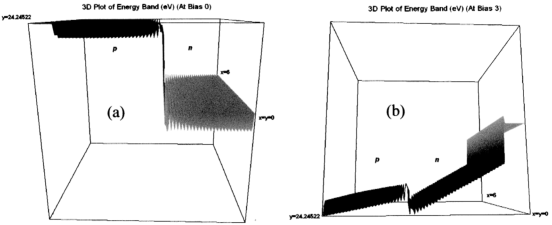

Figure 5.47: Energy band diagram with (a) no applied bias and (b) forward bias.

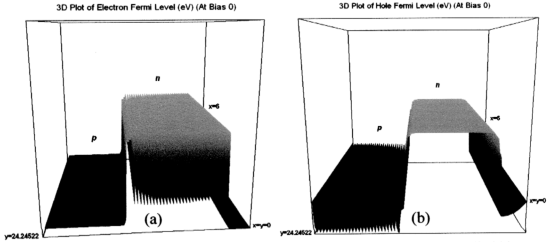

Figure 5.48: (a) Electron Fermi level and (b) Hole Fermi level with no applied bias.

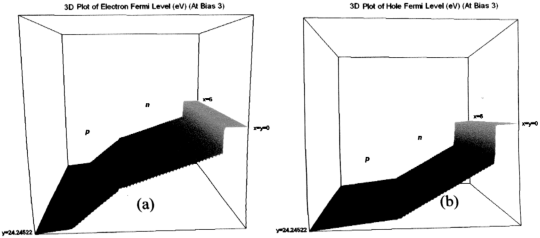

Figure 5.49: (a) Electron Fermi level and (b) Hole Fermi level with forward bias.

However, by employing heavy doping to the n- and p-regions also changed the Fermi level, E_F for these two regions. The normally constant and identical Fermi level at equilibrium split separately, forming the electron Fermi level, E_{Fe} and hole Fermi level,

E_{Fh} as simulated in 3D plot shown in Figure 5.48(a) and 5.48(b), respectively. Figure 5.49(a) and Figure 5.49(b) demonstrates that both the electron Fermi level and hole Fermi level are shifted when forward bias is applied. To give a better understanding, the energy band diagram of heavily doped p-n junction at equilibrium is schematically illustrates in Figure 5.50(a). When applying forward bias, the separation of the electron Fermi level and hole Fermi level is higher than the electron-hole recombination energy, *hf* in the narrow active region as shown in Figure 5.50(b). It is in this state that stimulated emission and lasing can occur because of the existence of excessive electrons and holes through the population inversion created by applying heavy doping to the n- and p-regions.

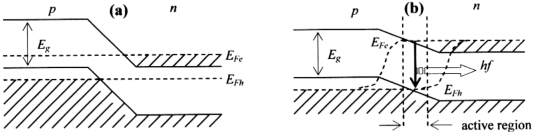

Figure 5.50: The heavily doped band diagram (a) at equilibrium and (b) with forward bias.

5.4.2 *1.55 μm VCSELs Diode Mode Analysis*

The mode analysis is done at the fundamental mode where the transverse and longitudinal modes are set to zero value [0, 0] for simulation. Figure 5.51 displays the contour plot of the fundamental mode with no bias applied with the horizontal cut is shown in Figure 5.52. It shows that the optical mode is overlapping the active region. The fundamental mode is simulated to confirm that the 1.55 μm VCSELs diode exhibit an optical mode at the active region for lasing to occur at the desired wavelength. This is visibly shown by the 3D plot of the mode profile in Figure 5.53.

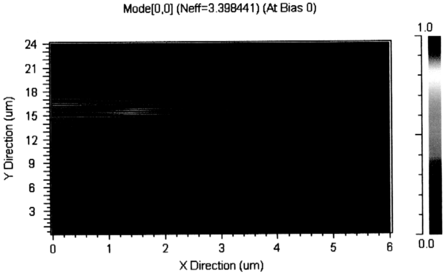

Figure 5.51: Fundamental mode profile as a contour plot for the 1.55 μm VCSELs.

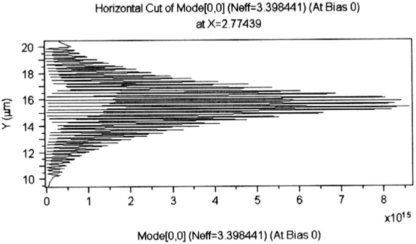

Figure 5.52: Horizontal cut of the fundamental mode profile for the 1.55 μm VCSELs.

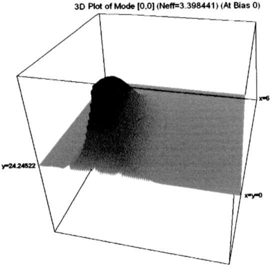

Figure 5.53: 3D plot of the fundamental mode profile for the 1.55 μm VCSELs.

When a bias of 4 volt is applied to the mode simulation, the 1.55 μm VCSELs diode emit a laser beam output. The near-field and far-field simulation can be done to characterize the profile of the laser beam emitted. Figure 5.54(a) shows the contour plot of the near-field characteristic with the 3D vertical cut is illustrated in Figure 5.54(b). The near-field characteristic simulation exhibits a symmetric and narrow laser beam profile is emitted from the active region of the device.

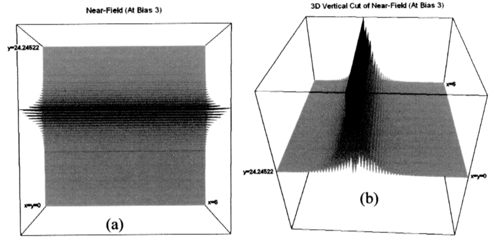

Figure 5.54: (a) Near-field contour plot and (b) in 3D plot for the 1.55 μm VCSELs.

As for the far-field characteristic, the far-field versus angle is plotted in contour plot as shown in Figure 5.55(a) with the 3D vertical cut is displayed in Figure 5.55(b). The angle corresponds to the lateral and transverse directions are used as measure of the emitted light angular spread and for determining the coupling efficiency between a laser diode and an optical fiber. It is given as below where $\Delta\theta$ is the angular spread, λ is the emission wavelength and s is the spot size [110].

$$2\Delta\theta = 0.64(\lambda/2s) \tag{5.7}$$

The simulation result demonstrates that the far-field distribution from the emitted VCSELs beam fits a Gaussian profile, with the peak located in the center and the profile is circularly symmetric. From equation (5.5) calculation, the angular spread is approximately 2.2^0 resulting in small beam divergence. This circular output beam with narrow beam divergence is readily coupled into optical fiber core which is generally circle in cross section. Thus, the 1.55 µm VCSELs diode is capable of achieving high coupling efficiency with the optical fiber or other external optics devices. It is also observed that the surface emission beam emitted is perpendicular to the wafer plane due to the VCSELs device geometry.

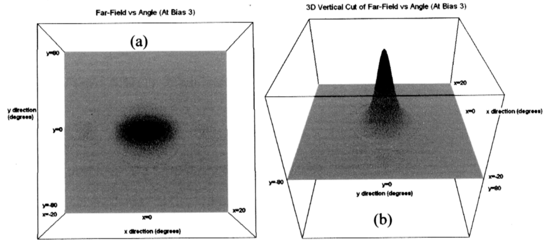

Figure 5.55: (a) Far-field vs. angle contour plot and (b) in 3D plot for the 1.55 µm VCSELs.

5.4.3 *1.55 µm VCSELs Diode PL Spectra*

Photoluminescence (PL) is a method where excess electron-hole pairs are excited with an optical source. This electron-hole pairs recombine where photons are emitted for radiative recombination type with the luminescent signals is detected as recombination occurs. Figure 5.56 demonstrates the PL spectra simulated at various carrier density, *N* and at room temperature, *T*=300K. As the carrier density becomes higher, the spontaneous emission occurs near the 1.55 µm wavelength. The peak is from the InGaAsP QW in the active region where it gives the lasing wavelength.

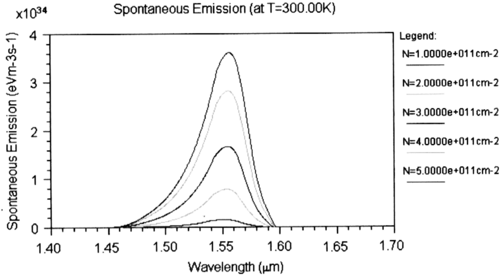

Figure 5.56: Photoluminescence (PL) spectra of the 1.55 µm VCSELs.

5.4.4 *1.55 µm VCSELs Diode Emission Spectrum*

The emission spectrum is simulated to investigate the lasing wavelength and the operation mode of the proposed 1.55 µm VCSELs diode. Figure 5.57 shows the optical spectrum simulated with a bias of 4 voltages and at room temperature.

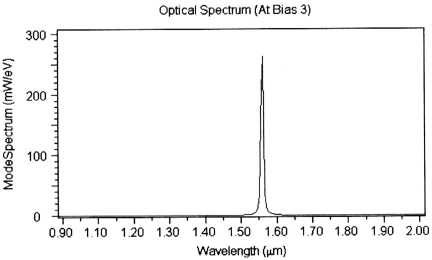

Figure 5.57: Optical spectrum of the 1.55 µm VCSELs.

The simulation result demonstrates that the proposed VCSELs diode operates with single longitudinal mode as exhibited by the single emission peak at 1.55 µm. In general, the mode spacing in laser diode is inversely proportional to the cavity length.

This indicates that the small cavity of VCSELs have large mode spacing. The longitudinal modes existing in a laser diode are functions of both the mode spacing and the material gain. In VCSELs, only one longitudinal mode coincides with the gain curve, resulting only one frequency wavelength is provided for lasing operation. This produces a narrow spectral width for VCSELs as shown in the result.

5.4.5 *1.55 μm VCSELs Diode L-I-V Characteristic*

The light-current-voltage (L-I-V) characteristic is simulated to investigate the electrical properties of the proposed 1.55 μm VCSELs diode. Figure 5.58 shows the L-I-V characteristic with a bias of 3 mA current is applied at room temperature.

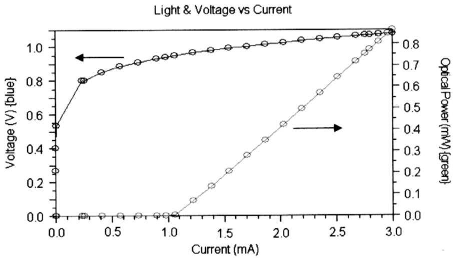

Figure 5.58: Light-current-voltage (L-I-V) characteristic of the 1.55 μm VCSELs.

From the L-I curve (green color), the threshold current, I_{th} is estimated at 1.05 mA. Threshold current density can be approximated as the ratio between the threshold current, I_{th} and the active region area, A given as

$$J_{th} = \frac{I_{th}}{A} \tag{5.8}$$

Higher output power with a linear increment is achieved when the input current is increased as more in-phase photons are generated. The slope of this linear L-I curve is used in the calculation of the differential quantum efficiency defined as [29]

$$\eta_D = \frac{dP/\hbar\omega}{dI/e} \cong \frac{dP}{dI}\frac{1}{E_g} \tag{5.9}$$

where e is the electron charge, E_g is the bandgap energy and $\hbar\omega$ is the photon energy. From this parameter, the power conversion efficiency is calculated as below [110], where η_D is the differential quantum efficiency and V_b is the voltage bias.

$$\eta_P = \eta_D \frac{E_g}{V_b}\left(1 - \frac{I_{th}}{I}\right) \tag{5.10}$$

Based on the threshold current estimated, the voltage at threshold, V_{th} is equivalent to 0.95 V, which is also correspond to the voltage across the VCSELs diode, V_D. Above threshold, the V-I curve (blue color) saturates since the splitting of the quasi-Fermi levels is clamped because the gain and the carrier density saturates [111]. The laser has two distinct voltage drops as illustrated in Figure 5.59, that is the voltage across the active region junction and the voltage across the series of resistors associated with the n- and p-DBR mirrors.

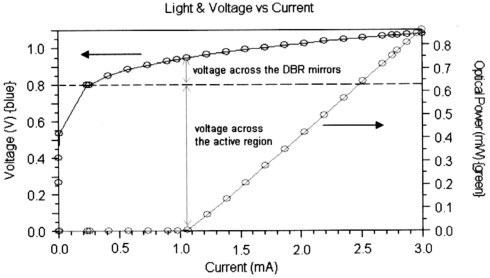

Figure 5.59: Voltage across of the active region and DBR shown in the L-I-V characteristic.

The turn-on voltage is estimated at 0.8 V, representing the voltage across the active region. This value is correspond to the bandgap energy value of the active region in eV (1.24/1.55 μm=0.8 eV). Thus, the voltage across the n- and p-DBR mirrors is 0.15 V. The series resistance of both DBR mirrors near threshold is given as [112]

$$R_{S-DBR} = \frac{(V_{th} - h\nu/e)}{I_{th}} \tag{5.11}$$

Table 5.10 displays the results from the L-I-V characteristic analysis of the 1.55 μm VCSELs diode simulation. The reported results of the highest performance 1.55 μm double-fused VCSELs [63] is also listed in the table as a comparison.

Table 5.10: The proposed 1.55 μm VCSELs diode simulation results in comparison with the highest performance 1.55 μm Double-fused VCSELs.

Parameters	Proposed 1.55 μm VCSELs Diode	1.55 μm Double-fused VCSELs [63]
Threshold current, I_{th} (mA)	1.05	0.80
Threshold current density, J_{th} (kA/cm^2)	1.53	1.00
Differential quantum efficiency, η_D (%)	0.56	Not reported
Power conversion efficiency, η_P (%)	0.28	Not reported
Voltage at threshold, V_{th} (V)	0.95	2.10
Turn-on voltage (V)	0.80	0.80
DBR series resistance, R_{S-DBR} (Ω)	143	Not reported

The threshold current of 1.05 mA simulated by the proposed 1.55 VCSELs diode is relatively among the lowest in various reported work demonstrated for 1.55 μm wavelength VCSELs. The lowest demonstrates by the 1.55 μm double-fused VCSELs [63] is achieved by utilizing oxide aperture layer as current confinement scheme. In general, VCSELs exhibits low threshold current for operation, thus the threshold current density is lower in comparison to the EELs due to the small volume of the active region. It must be born in mind that the threshold current density calculated in equation (5.6) is only an approximation, by assuming that all the injected current passes through the active region. In actual device, the equation is more complex as given in [113]. This is because the existence of leakage current is not calculated in the software. Nevertheless, it is still a useful value for comparison purposes. The differential quantum efficiency obtained from the simulation is 0.56. This parameter defined as the ratio of the increase in the number of output photons for a given increase in the number of injected electrons, is a measure of the electrical-to-optical conversion efficiency. As for the power conversion efficiency or wall-plug efficiency in other term, the proposed 1.55 μm VCSELs diode achieved 0.28 efficiency. Typically, VCSELs exhibits 0.3 and 0.1 for the differential quantum efficiency and power conversion efficiency, respectively [114]. The proposed device shows improvement in threshold voltage with the turn-on voltage indicates a similarity because both active regions employed same bandgap energy to achieve the 1.55 μm emission wavelengths. As for the DBR series resistance, the proposed 1.55 μm VCSELs diode demonstrates high series resistance, much higher than the few ohms for a typical EELs. The high series resistance of the DBR mirrors originates from the steep energy barriers at the heterojunctions of DBR. This resistance is especially large for p-DBR mirror since it is very difficult for the holes to climb up these barriers due to the hole large effective mass. Combined with the small cavity volume of VCSELs, this high series resistance generates significant heat which leads to the device self-heating. This is a common problem in most VCSELs. Also, the high series resistance calculated is due to the idealized doping profile adopted in both the n- and p-DBR mirror simulation. More realistic doping profiles such as pulsed doping or delta-doping at the interfaces if simulated by the software will probably produce a lower DBR series resistance.